Journal of Physics D:
Applied Physics

Numerical investigation of atmospheric positive diffuse discharge mode transition: the effect of voltage rise time

To cite this article before publication: Yulin Guo *et al* 2025 *J. Phys. D: Appl. Phys.* in press https://doi.org/10.1088/1361-6463/ae1597

Numerical Investigation of Atmospheric Positive Diffuse Discharge Mode Transition: The Effect of Voltage Rise Time

Yulin Guo[1,2], Yaqi Zhang[1], Yifei Zhu[1], Pascal Jeanney[2], Alexandra Brisset[3], Anbang Sun[1,*] and Pierre Tardiveau[2,*]

[1]School of Electrical Engineering, Xi'an Jiaotong University, State Key Laboratory of Electrical Insulation and Power Equipment, Xi'an, 710049, China

[2]Laboratoire de Physique des Gaz et des Plasmas, CNRS, Universite Paris-Saclay, Orsay 91400, France

[3]Laboratoire EM2C, CNRS, CentraleSupélec, Univeristé Paris-Saclay, Gif-sur-Yvette cedex 91192, France

E-mail: anbang.sun@xjtu.edu.cn and pierre.tardiveau@universite-paris-saclay.fr

Abstract

This work computationally investigates the morphological transition of atmospheric pressure positive nanosecond pulsed discharges from a diffuse to a multi-channel regime. Using 2D fluid models – specifically the Local Field Approximation (LFA), a flux-corrected LFA, and the Local Mean Energy Approximation (LMEA) – we analyze the influence of voltage amplitude and rise time on discharge dynamics. Results reveal that a short voltage rise time (2 ns) consistently produces a diffuse discharge(from 56 kV to 85 kV amplitude), which exhibits significant acceleration at higher voltages but constant-velocity at a lower voltage(56 kV), in agreement with experimental observation. Both flux-corrected LFA and LMEA better match experimental results regarding discharge width and average development velocity, with LMEA showing a generally longer inception delay and faster development velocity. Conversely, for slower rise times (5.8 ns), the standard LFA model predicts off-axis branching especially under lower voltage(56 kV). In contrast, both the flux-corrected LFA and LMEA models successfully capture the development of a main channel alongside branching structures. Notably, the flux-corrected LFA model exhibits the best qualitative agreement with experiments, demonstrating the suppression of branching at higher voltages. Although limited by its 2D framework, the model provides results comparable to those of 3D models, clarifying the model-dependent nature of simulated discharge morphologies and

offering critical insights into the physical mechanisms driving the diffuse-to-branched transition.

1. Introduction

Positive diffuse discharge is a special type of streamer discharge characterized by a diffusive morphology, generated by high-amplitude, short-nanosecond pulse rising edges. This uniform and highly repeatable discharge, which can be produced at atmospheric pressure, holds promising views and prospects for both fundamental research and industrial applications. Yet as pointed out in the work of Tardiveau et al.[1], the discharge morphology is strongly related to the voltage rise time: as the pulse rise time increases, the diffuse discharge transitions from a 'diffuse regime' to a 'multi-channel regime', thereby losing its unique characteristics.

Addressing the influence of discharge rise time on discharge characteristics, Briels et al. [2, 3] conduct a series of experiments on the impact of voltage rise time on atmospheric positive filamentary streamers. They found that as the voltage increases and the rise time decreases, both the diameter and the development velocity of the streamer increase, and an empirical mathematical relationship exists: $v=0.5d^2$ $mm^{-1}ns^{-1}$. Similar patterns are experimentally found to also apply to the inception cloud[4-7], which is a propagation mode with a special morphology that lies between streamer inception and branched filaments, but its diameter is larger than that of filamentary streamers. It should be noted that these studies on filament streamers and inception clouds mostly use voltage amplitudes of 10-60 kV, rise times above 15 ns, and gaps of 4-16 cm. Thus difficult to form the diffuse discharge morphology described previously; instead, they remain in the 'multi-channel regime'. Tardiveau et al.[1, 8] investigate diffuse discharges generated in short gaps (10-20 mm) by voltages with high amplitudes (above 50 kV) and short nanosecond pulse rise times (2-5 ns). They find that in the 'diffuse regime,' diffuse discharges also exhibit the same pattern: as the rise time decreases and the amplitude increases, the discharge develops faster and has a larger diameter. The explanation for this phenomenon is achieved through 2D axisymmetric fluid simulations. The most classic of these are the simulations by Komuro et al. [9] for filamentary streamers and by Bourdon et al.[10] for diffuse discharge, respectively. The former uses voltages with amplitudes of 18-25 kV and rise times of 46-218 ns to simulate a single filament streamer discharge at atmospheric pressure within a 13 mm gap. The latter employs voltages with an amplitude of 55 kV and rise times of 0.5-1.5 ns to simulate diffuse discharge at atmospheric pressure within a 16 mm gap. They offer a consistent explanation for the same phenomenon: the electric field reaching the breakdown threshold in a shorter time accelerates the expansion of the ionization region, especially due to the increase in the radial electric field component caused by elevated local charge density. Similarly, in the work of Marode et al.[11], Brisset et al.[12], and Zhu et al.[13], they use different fluid models to discuss the evolution of the electric field during discharge development, and achieve good agreement with experiments, but focus more on the 'diffuse regime'. However, these simulation work neglect to explain another important phenomenon: why diffuse discharge transitions from a 'diffuse regime' to a 'multi-channel regime' as the voltage rise time decreases.

For filament streamers, Teunissen et al. [14] reproduce the process where the inception cloud destabilizes into streamers during the development of positive streamer discharge using

a 3D PIC-MCC model. They also quantitatively simulate the process of positive streamer branching with a 3D fluid model that includes Monte Carlo photoionization[15], correctly predicting important information such as the number of branches and angles. Their simulation work reveals that stochastic processes and Laplacian instability are the causes of positive streamer branching under low voltage and slow rise times. Although they fully simulate how filament streamers emerge from the inception cloud, a specific explanation for the huge morphological differences under different rise times is still lacking. Especially, the reason for the discharge mode transition in diffuse discharge caused by different rise times still requires further discussion.

In this work, we primarily focus on the 'diffuse regime' and 'multi-channel regime' of atmospheric pressure positive nanosecond pulse discharge under different voltage amplitudes and rise times. We attempt to explain, through a fluid simulation model, why a reduction in rise time of approximately 3 ns causes such a significant difference in discharge mode. In Section 2, we introduce the numerical method used in this paper. In Section 3, we discuss the causes of diffuse discharge and filamentary streamers under different rise times. We also make different corrections to the model to investigate the differences between the specific discharge characteristics obtained from simulation and those from experiments.

2. Numerical Method

The model we use in this work is a classic 2D fluid model with local field approximation(LFA) and local mean energy approximation (LMEA). The LFA part of this model has been validated through comparison with high-pressure SDBD experiments [16], and the LMEA part has been validated through moderate-pressure fast ionization wave experiments [17]. Besides, the model has been used to calculate diffuse discharge at atmospheric[13] and low pressure[18], and achieved good agreements with experiment results. Thus, here we do not reiterate the mathematical equations of the model.

The specific geometric configuration adopted for the simulation is shown in Fig. 1 below. The calculation domain is 50mm×50mm. This calculation domain is chosen because further increasing it does not significantly affect the simulation results. Conversely, reducing this boundary further to below 30 mm begins to influence the discharge volume itself. The red region represents the high-voltage electrode with the pin positioned at Z=16 mm, and the ground plane electrode is located at Z=0 mm. The electrode geometry is identical to that used in the experiment, with specific geometric parameters labeled in the figure. Within the darker gray area, which serves as the plasma computational domain, only the continuity equations are solved. The Helmholtz equation for photoionization and the Poisson equation for the electric field are solved throughout the entire 50 mm×50 mm domain.

Boundary conditions for Poisson's equation are set as Dirichlet on the electrode and as Neumann on the outer computational domain boundaries, away from the immediate plasma vicinity. In addition, the ghost fluid method [19] is employed on the electrode surface to avoid potential serration shape. Concerning the drift-diffusion equation, we implement zero-flux and homogeneous Neumann conditions for both positive and negative species at the anode, while reversing these conditions at the cathode. A crucial constraint is the zero radial flux enforced for all charged species along the central axis. The simulation begins with a neutral background, where initial densities for both electrons and positive ions are set at 10^{10} m^{-3}. The positive ions

include a uniform distribution of 0.2×10^{10} m^{-3} O_2^+ and 0.8×10^{10} m^{-3} N_2^+. All other species are set to zero. In addition, a Gaussian electron density distribution is set at Z=15. 75mm, with a peak density of 10^{17} m^{-3} and a radius of 0.25 mm. Gas temperature and pressure are set at 300 K and 101325 Pa throughout the entire calculation domain, with the gas mixture comprising an 8:2 mixture of N_2:O_2.

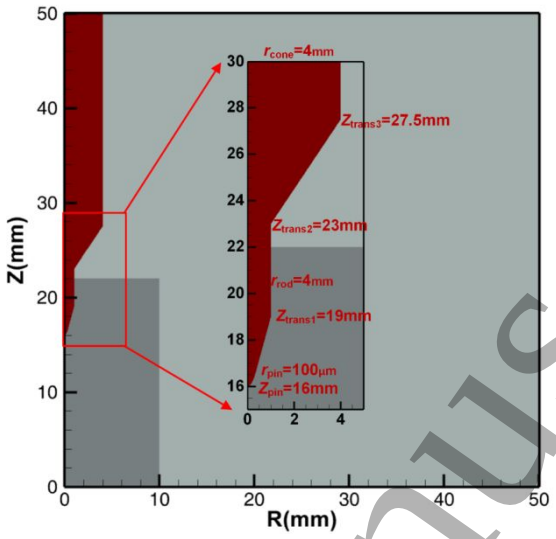

Fig. 1 Simulation configuration used in this work.

A simple chemical reaction system is considered in this work based on the simulation work of [20], in which they focused on the stagnating positive streamers with a high electric field at streamer tip, and more recombination reactions(R14-R25) are added based on their work.

Table 1 Reaction system used in the simulation*

	Reaction	Reaction rate	Ref
R1	$e+N_2 \rightarrow N_2^+ + e + e$	$f(\sigma, E/N)$	[21]
R2	$e+O_2 \rightarrow O_2^+ + e + e$	$f(\sigma, E/N)$	[22]
R3	$e+O_2+O_2 \rightarrow O_2^- + O_2$	$f(E/N)$	[22]
R4	$e+O_2 \rightarrow O^- + O$	$f(E/N)$	[22]
R5	$O_2^- + M \rightarrow e + O_2 + M$	$f(E/N)$	[23]
R6	$O^- + N_2 \rightarrow e + N_2O$	$f(E/N)$	[23]
R7	$O^- + O_2 \rightarrow O_2^- + O_2$	$f(E/N)$	[23]
R8	$O^- + O_2 + M \rightarrow O_3^- + M$	$f(E/N)$	[23]
R9	$N_2^+ + N_2 + M \rightarrow N_4^+ + M$	$5\times10^{-29}\times(300/T_{gas})^2$	[24]
R10	$O_2^+ + O_2 + M \rightarrow O_4^+ + M$	$2.4\times10^{-30}\times(300/T_{gas})^3$	[24]
R11	$N_4^+ + O_2 \rightarrow O_2^+ + N_2 + N_2$	2.5×10^{-10}	[24]
R12	$e+O_4^+ \rightarrow O_2 + O_2$	$1.4\times10^{-6}\times(300/T_{gas})^{0.5}$	[24]
R13	$e+N_4^+ \rightarrow N_2 + N_2$	$2\times10^{-6}\times(300/T_{gas})^{0.5}$	[24]
R14	$N_2^+ + O^- \rightarrow N + N + O$	10^{-7}	[24]
R15	$N_2^+ + O_2^- \rightarrow N + N + O_2$	10^{-7}	[24]
R16	$N_2^+ + O_3^- \rightarrow N + N + O_3$	10^{-7}	[24]

R17	$O_2^+ + O^- \rightarrow O+O+O$	10^{-7}	[24]
R18	$O_2^+ + O_2^- \rightarrow O+O+O_2$	10^{-7}	[24]
R19	$O_2^+ + O_3^- \rightarrow O+O+O_3$	10^{-7}	[24]
R20	$O_4^+ + O^- \rightarrow O_2+O_2+O$	10^{-7}	[24]
R21	$O_4^+ + O_2^- \rightarrow O_2+O_2+O_2$	10^{-7}	[24]
R22	$O_4^+ + O_3^- \rightarrow O_2+O_2+O_3$	10^{-7}	[24]
R23	$N_4^+ + O^- \rightarrow N_2+N_2+O$	10^{-7}	[24]
R24	$N_4^+ + O_2^- \rightarrow N_2+N_2+O_2$	10^{-7}	[24]
R25	$N_4^+ + O_3^- \rightarrow N_2+N_2+O_3$	10^{-7}	[24]

*Unit of rate constants are s^{-1}, $cm^3\ s^{-1}$, and $cm^6\ s^{-1}$.

The three applied voltage profiles used in this paper are shown in Fig. 2. Among these, CH1 has a rise time $T^{10\%-90\%}$ of 2 ns, CH2 has a rise time of 2.95 ns, and CH3 has a rise time of 5.2 ns. To observe the effect of different rise times in the simulation, the starting points of all voltage profiles are aligned to 8% of their peak value (t=0ns).

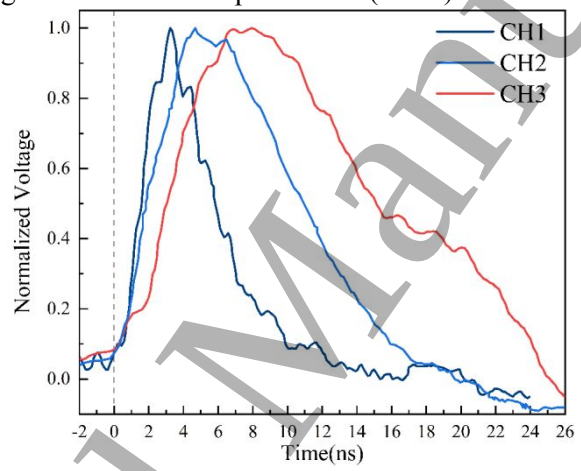

Fig. 2 The three voltage profiles with different rise times used in this work.

3. Results and discussion

3.1 The effect of rise times on the discharge morphologies in the experiment

As reviewed above, in discharge experiments, the rise time of the applied voltage significantly determines the discharge morphology. As illustrated in Fig. 3: when a 2 ns (CH1) rise time is employed, the discharge consistently maintains a diffusive morphology across various voltage amplitudes (56kV-85kV). When the rise time is slightly reduced to 2.95 ns (CH3), similarly, the discharge consistently remains in a diffuse state. The only difference is that its maximum width is smaller compared to CH1. These are the 'diffuse regime' described in [1]. In contrast, with a 5.2 ns (CH3) rise time, a branched discharge tends to form, particularly at lower voltage amplitudes. Additionally, for CH3, a main discharge channel, beneath the pin electrode, is consistently observed alongside branched streamers developing along electric field lines. This is the so-called 'multi-channel regime'. With increasing voltage amplitude, this main channel widens, and the count of branched streamers reduces. Ultimately, only the main channel persists at 85 kV, but its morphology is not a conical diffuse form, but rather more closely resembles a single, streamer-like discharge filament.

It should be noted that all these experimental images are obtained at a discharge repetition

frequency of 10 Hz. However, through experimentation, we find that the discharge frequency does not significantly affect these branching patterns caused by the rising edge. This is especially true when the discharge repetition frequency is reduced to 1 Hz and 0.05 Hz; the branching phenomenon under CH3 remains pronounced.

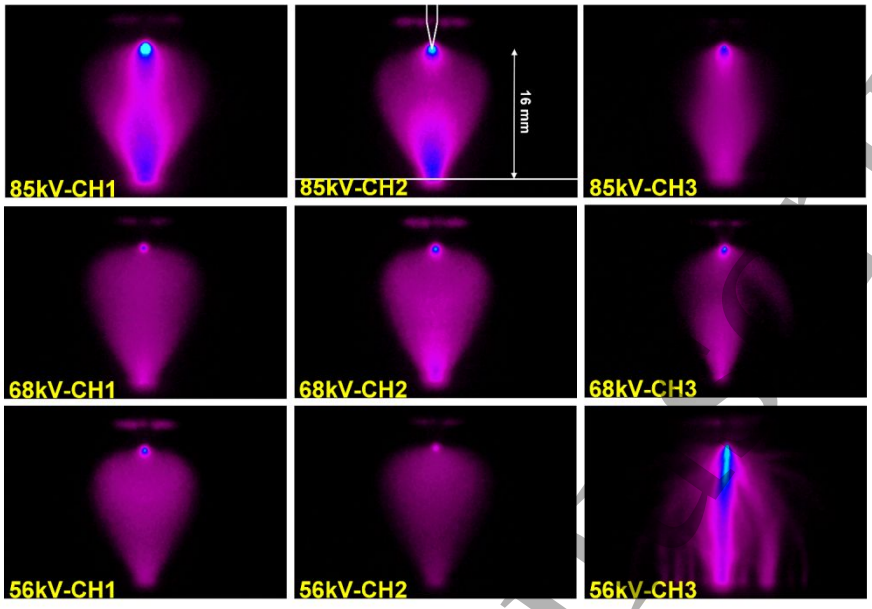

Fig. 3 The discharge morphologies under different rise times in the experiment. The gate used to capture the images is 0.5 ns.

Within our 2D axisymmetric fluid model in Section 3.2, we attempted to simulate the discharge morphology under different voltage rise times and sought to elucidate why a slower rise time process leads to discharge branching in these cases.

3.2 Modeling on the discharge morphology transition under different rise times

3.2.1 LFA modeling on the rise time effect

Since the discharge morphology observed under a 2.8 ns rise time (CH2) closely resembles that of the 2.0 ns case (CH1)-both presenting a conical diffusive shape-the comparative analysis in our simulation focuses on the 2.0 ns (CH1) and 5.2 ns (CH3) rise times.

Fig. 4 illustrates the temporal evolution of the electron density distribution obtained from the 2D axisymmetric fluid simulation under the 2.0 ns rise time(CH1). It can be observed that, in addition to the main discharge region below the pin tip (which first develops spherically and then conically), two 'parasitic streamers' exist on the pin surface. The upper one is generated due to electric field enhancement caused by a local protrusion formed as the pin electrode transitions from conical to cylindrical; it is called a 'side flare' in [13] and is also found in experiments and simulations in [18]. The lower parasitic streamer originates from the surface of the conical region of the pin, and its generation is due to the Laplacian field caused by the special shape of the pin electrode. In [25], this situation is improved by employing a rod electrode instead of a pin and a disc holder above the electrode. However, in this paper, to maintain consistency with the experiment, we still use the electrode structure that is 1:1 with the experimental electrode. Subsequent analysis of the discharge completely ignores these two parasitic streamers and only discusses the discharge generated below $Z = 16$ mm.

With increasing applied voltage amplitude, the discharge propagates faster, and the time for it to reach the plane electrode is reduced, where the discharge required 4.9 ns to reach the plane

electrode at 56 kV, while at 85 kV, this time is reduced to 2.7 ns. Correspondingly, the average propagation velocity increases from 3.27 mm/ns to 5.93 mm/ns. The maximum discharge width also exhibits a slight increase. When defining the discharge profile by the10^{18} m^{-3} electron density contour line (the black line in Fig. 4), the width grows from 12.35 mm at 56 kV to 13.38 mm at an 85 kV peak. This is consistent with the simulation results of Bourdon et al.[10] reviewed above.

Fig. 5 presents the temporal evolution of the reduced electric field (E/N) on-axis. The electric field at the head of the discharge increases with increasing applied voltage amplitude. Specifically, when the discharge reaches the mid-gap point (8 mm), the peak head E/N increases from 409 Td at 56 kV, to 459 Td at 68 kV, and further to 526 Td at 85 kV. Additionally, the discharge propagation velocity is also voltage-dependent: while it exhibits nearly constant velocity at 56 kV (with only minor acceleration around 4.5 ns, as seen in the head trajectory), it undergoes pronounced acceleration at higher voltages. This acceleration begins around 2.5 ns (propagates to Z=8 mm) at 68 kV and around 2.0 ns (propagates to Z=8 mm) at 85 kV. Such abrupt acceleration after passing the mid-gap at high applied voltages is also consistent with the experimental findings of Tardiveau *et al*. [1].

A new, not fully explained problem emerges here: Why does diffuse discharge at 56 kV develop at a constant velocity (except when it develops very close to the plane electrode), while discharge at 68 kV and 85 kV begins to accelerate significantly after crossing Z=8 mm? At this position, the discharge head is still very far from the plane electrode, and the electric field does not show significant enhancement. We believe this relates to the stability field during the discharge development process, which is defined as the homogeneous electric field in which a streamer can propagate with stable width and velocity. This means whether the discharge accelerates or not is unrelated to the value of its head electric field, but rather is related to the background electric field it is in. However, in this work, during the diffuse discharge development, the value of the background electric field at the discharge head changes with time, rapidly. Therefore, one cannot simply use the background electric field at a certain moment as a reference. Instead, we consider the internal electric field of the discharge, E_{ch}, for estimation, following the method mentioned in [26]. The E_{ch} of the diffuse discharge (i.e., the electric field in the light blue triangular region above the discharge head in Fig. 5), under the three voltage amplitudes, has average values of 5.75 kV/cm (23Td), 11.25 kV/cm (45Td), and 13.75 kV/cm (55Td), respectively. According to the calculations by Francisco *et al*.[27], the corresponding homogeneous stability field during positive streamer propagation is 4.65 kV/cm. The larger the background electric field is compared to this value, the greater the acceleration during streamer propagation and the faster the streamer width increases. The 56kV amplitude result is closer to the homogeneous stability field in ambient air. Therefore, it maintains nearly constant velocity development. In contrast, at higher amplitudes, the discharge acceleration process is more pronounced.

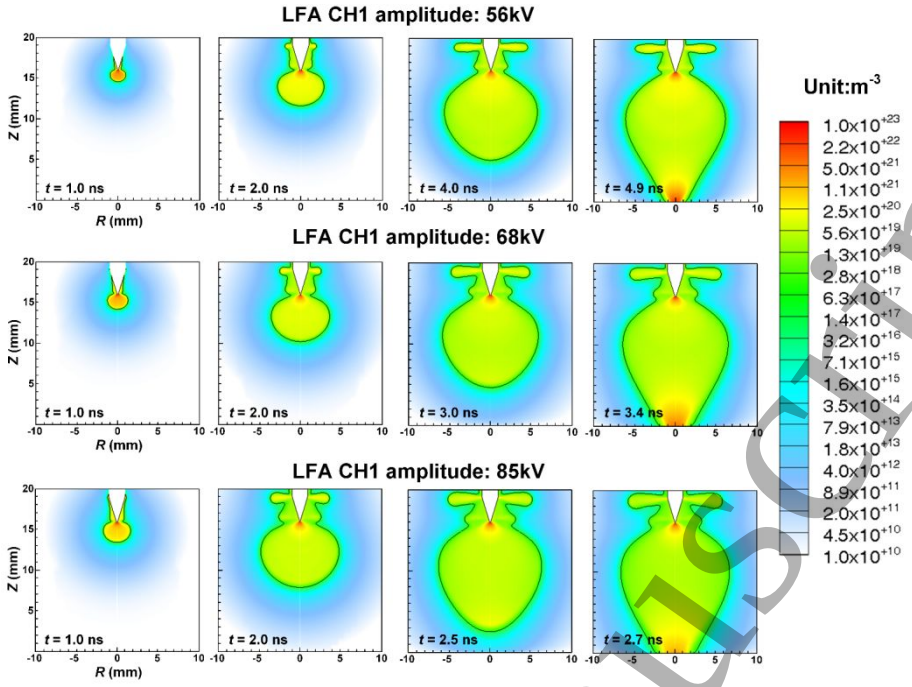

Fig. 4 Electron density distribution under different voltage amplitudes at CH1(2 ns rise time).

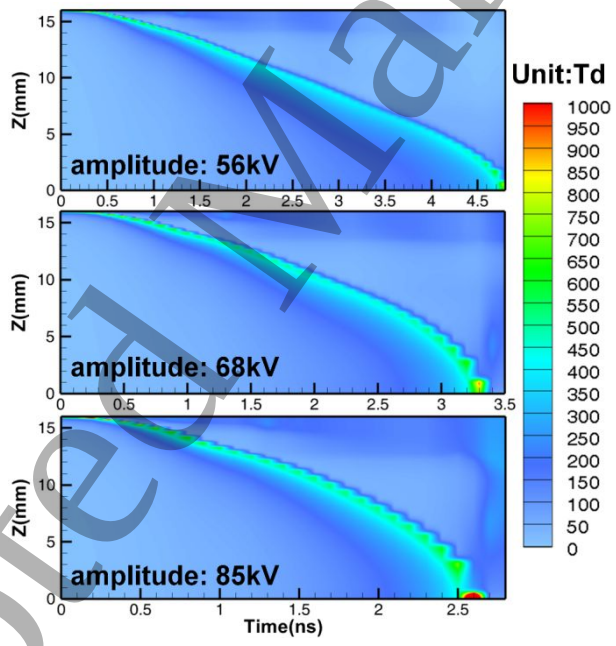

Fig. 5 Reduced electric field distribution on the axis under different voltage amplitudes at CH1(2 ns rise time).

However, when the rise time is adjusted to 5.2ns (CH3) in the simulation, a completely different discharge pattern from CH1 appears. Fig. 6 shows the electron density evolution for 5.2 ns rise time (CH3) discharges under different voltage amplitudes. While initial propagation occurs along the symmetry axis towards the plane electrode, a distinct off-axis development begins when the discharge head reaches Z=14 mm, redirecting propagation into the R direction. Subsequently, the axial discharge component ceases, and the radially developing discharge traverses the remaining gap to the plane electrode. This off-axis branching pattern is

consistently observed at all three voltage amplitudes, while increases in peak voltage accelerate the propagation and broaden the branched discharge. Defining the discharge by the 10^{18} m^{-3} electron density contour line(black line in Fig. 6), the maximum width expands from 3.57 mm (56 kV) to 4.15 mm (68 kV) and 4.95 mm (85 kV).

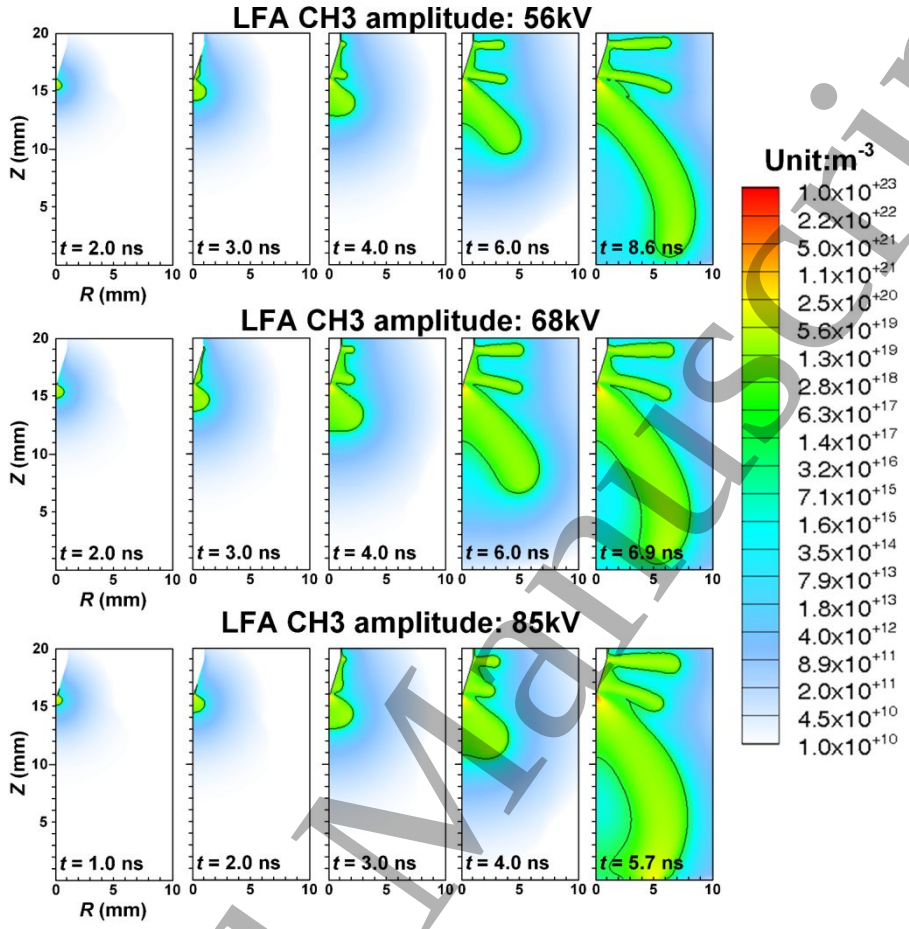

Fig. 6 The electron density distribution under different voltage amplitudes in CH3(5.2 ns rise time).

The evolution of the reduced electric field during the discharge development process for two different rise times is shown in Fig. 7. With the short rise time (CH1), the location of the maximum electric field at the discharge head continuously stays close to the symmetry axis. However, under the longer rise time (CH3), as the discharge developed to about 14.4 mm (at t=3.0 ns), the peak electric field's position at the head had already clearly shifted away from the symmetry axis. Comparing these simulation results with the experimental results, two issues are apparent: 1) The simulation lacks a main discharge channel developing along the symmetry axis. 2) In the simulation, the discharge at 85 kV still branches, whereas in the experiment, it does not.

The reason for this lies in a deficiency of the LFA model: when electrons diffuse parallel to the electric field, the LFA fails to fully capture their rapid energy loss process, consequently causing electrons to diffuse and ionize towards regions of high electric field strength. As noted in [28], this is a diffusion phenomenon often observed in high electron density regions bordered by strong electric fields above breakdown. Modifications based on this LFA model will be discussed in the next Sections.

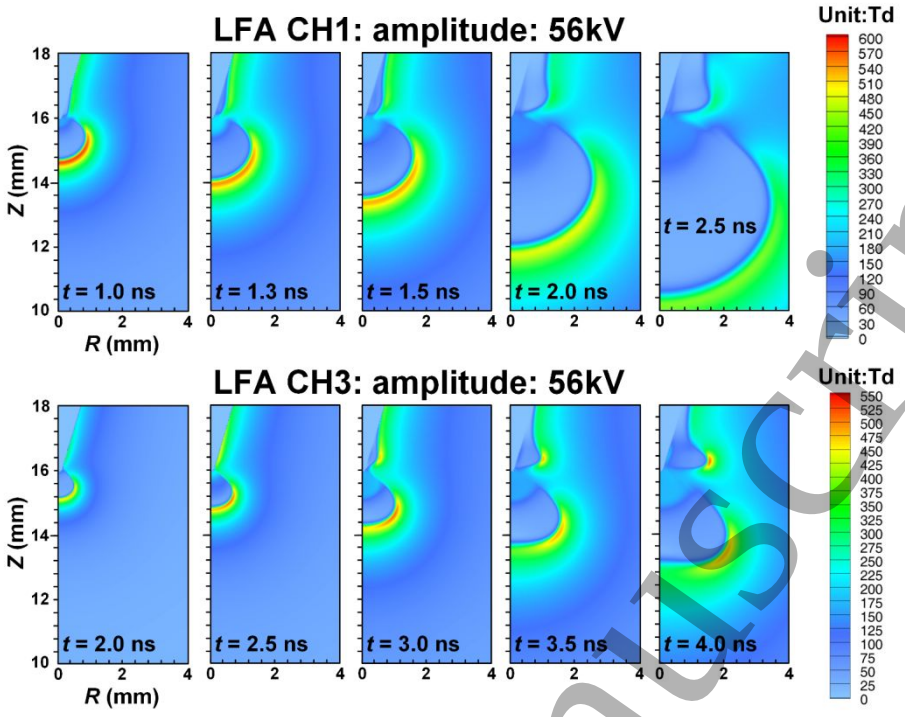

Fig. 7 The reduced electric field evolution under different rise times.

3.2.2 Investigation of the seed electron distribution

The simulated off-axis results presented in Section 3.2.1 are obtained under initial conditions with seed electrons at a density of 10^{17} m^{-3} within a small, localized region beneath the pin tip, supplemented by a uniform background ionization of 10^{10} m^{-3}. When the spatial extent of the seed electron distribution is increased, the main discharge, which is absent in Fig 6, shows up: By modifying the seed electron distribution from a circular area (0.25 mm radius) to an elliptical shape elongated in the Z-direction (3 mm length) while maintaining the original *R*-direction extent(0.25 mm), with a constant density of 10^{17} m^{-3}, we present the corresponding simulation results in Fig. 8. Even though the main discharge advances along the symmetry axis, following the seed electron distribution region, a branch that deviates from the main discharge still originates from it during the initial phase (t<3.0 ns) and develops simultaneously. An artificially introduced small, low-ionization region proved insufficient to inhibit the generation of additional branching beyond the main discharge. Nevertheless, the simulation results show better agreement with the experimental findings.

A high-density initial seed distribution of this shape physically represents either a highly pre-ionized channel before discharge inception or the generation of minute streamer discharges before the discharge inception. Given that the discharge frequency used in the experiment is 10 Hz, resulting in a 100 ms interval between adjacent discharges, there is sufficient time for electrons to recombine and attach. Therefore, it is unlikely that a highly pre-ionized channel would still exist. However, it should be noted that due to the unique voltage waveform, the pin electrode remains at 2-4 kV for approximately 10 ns before the 5.8 ns rising edge. Consequently, a local electron avalanche can occur, potentially generating electrons with a density of 10^{17} m^{-3} (or less) distributed over a relatively large area. It is possible that this avalanche process is weak and its ionization degree is low. Therefore, experiments cannot capture this very faint luminous process.

Therefore, it is possible for main discharge and discharge branching to occur in the experiment due to the distribution of seed electrons.

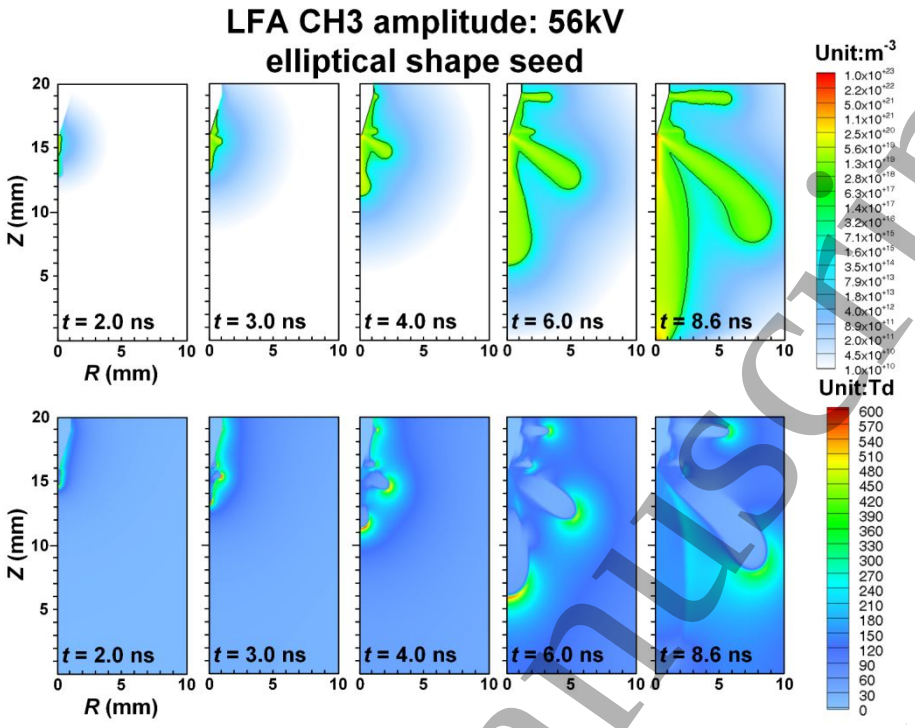

Fig. 8 Electron density and reduced electric field evolution under the 10^{17} m^{-3} elliptical shape seed in CH3.

Further expanding the seed electron distribution to a 10^{17} m^{-3} circular Gaussian distribution with a 3 mm radius (covering the branching starting location in Fig. 6), the discharge branching vanished. The reduced electric field distribution is shown in Fig. 9. The discharge is limited to a single main channel, which maintains its position along the symmetry axis throughout its development. It is crucial to highlight, however, that this simulation is inconsistent with the experimental observations. This discrepancy arises because, given the experimental 10 Hz repetition rate, such a high-density, wide-ranging seed distribution is highly improbable. Moreover, the previously discussed avalanche is also incapable of generating electrons distributed over such a broad area.

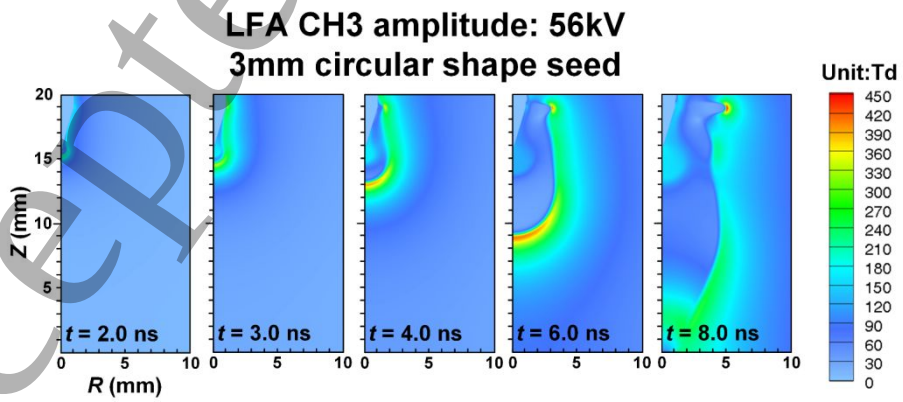

Fig. 9 Reduced electric field evolution under the 10^{17} m^{-3} 3mm circular round shape seed in CH3.

3.2.3 Investigation into the Introduction of Correction Factors for the LFA Model

The primary concern regarding this phenomenon observed in the simulations is to exclude numerical instability as a cause. Consequently, extensive testing is performed, including grid refinement near the axis (Z=8-16 mm, R=0-5 mm, with mesh sizes from 1 μm to 5 μm) and analysis of the continuity equation's reaction source terms, the phenomenon persisted.

A second concern is whether, under these conditions, the LFA no longer satisfies its limitations. According to [29], the condition for the LFA limitations to hold is as shown in equation 1, in which λ is the energy dissipation length. By calculating the terms on both sides of this equation in the simulation, it is found that this condition consistently holds throughout the discharge development process and the maximum reduced electric field does not exceed 1000 Td. Therefore, the LFA applicability condition is always satisfied. However, LFA can give unphysical results when the mentioned validity condition is fulfilled.

$$\frac{1}{\lambda(z,\varepsilon,t)} ? \frac{1}{E(z,t)}\partial_z E(z,t) \qquad (1)$$

Thus we consider the observation by Soloviev and Krivtsov [30] that strong electron density and field gradients can invalidate the local field approximation (LFA), potentially causing electric field enhancement and further unphysical streamer behavior: the diffusive electron flux parallel to the electric field (thus corresponding to a loss of energy) should not contribute to impact ionization. That is to say, the LFA cannot simulate the 'electron energy cooling process' caused by the electric field. Their proposed solution involves applying a correction factor, f_ε, to the collisional ionization source term, as formulated below in equation (2). Within this equation, $\hat{\mathrm{E}}$ signifies the electric field unit vector. Γ^{diff} and Γ^{drift} correspond to the electron diffusive and drift fluxes, respectively, with f_ε being restricted to the range of [0, 1].

$$f_\varepsilon = 1 - \frac{\hat{\mathrm{E}}\cdot\Gamma^{\mathrm{diff}}}{\mathrm{P}\Gamma^{\mathrm{drift}}\mathrm{P}} = 1 + \frac{\hat{\mathrm{E}}\cdot(D_e\nabla n_e)}{\mu_e n_e |E|} \qquad (2)$$

Further, as reviewed in the work of Teunissen [28], there is another method that can be used to modify the source term near a strong gradient, called the full flux source scheme. Introducing an effective factor g, given in Table 2, to prevent electrons from generating new ionization. Following this method, the ionization source term is further modified, and the results are given in Fig. 10, hereinafter, it is denoted as LFA(g). Upon introducing the effective factor g[0,1], a main discharge channel is established and maintained along the axis, and discharge branching is noticeably suppressed compared with the results in Fig. 6. Under 56 kV, the discharge near the pin electrode is initially compact, showing limited radial spread. This radial component intensifies as the discharge propagates, leading to a clear separation between the main discharge and branched channel by the time the main discharge arrives at the plane electrode (6.8 ns); the branch persists even after the main discharge has reached the plane electrode. This behavior is also observed under 68 kV, where the main discharge-branched channel separation is also evident upon its arrival at the plane electrode (5.8 ns). However, at 85 kV, the discharge reaches the plane electrode (5.0 ns) without significant branching. The evolution of the reduced electric field during discharge development at 56 kV and 85 kV is depicted in Fig. 11. At t=4.0 ns, discharges at both amplitudes presented two peaks in the electric field: one peak at the head along the symmetry axis and another on the right flank of

the discharge profile. With further discharge development, the two electric field peaks at 56 kV amplitude exhibited more pronounced separation, resulting in the formation of a distinct branch. In contrast, at 85 kV amplitude, although the two regions of the discharge's electric field also showed some divergence, the separated 'branch' on the right possessed a wider head, thus making it appear still integrated with the main discharge. Ultimately, even after the main discharge propagates to the plane electrode (t=5.4 ns), the right-side branch continues to develop.

Table 2. The effective factor

Relation between advective and diffusive flux	effective factor
balance each other	$g = \|\Gamma\| / \|\Gamma^{\text{drift}}\|$
parallel	f_ε
opposite direction	$g = 1 - \|\Gamma^{\text{diff}}\| / \|\Gamma^{\text{drift}}\|$
orthogonal	1

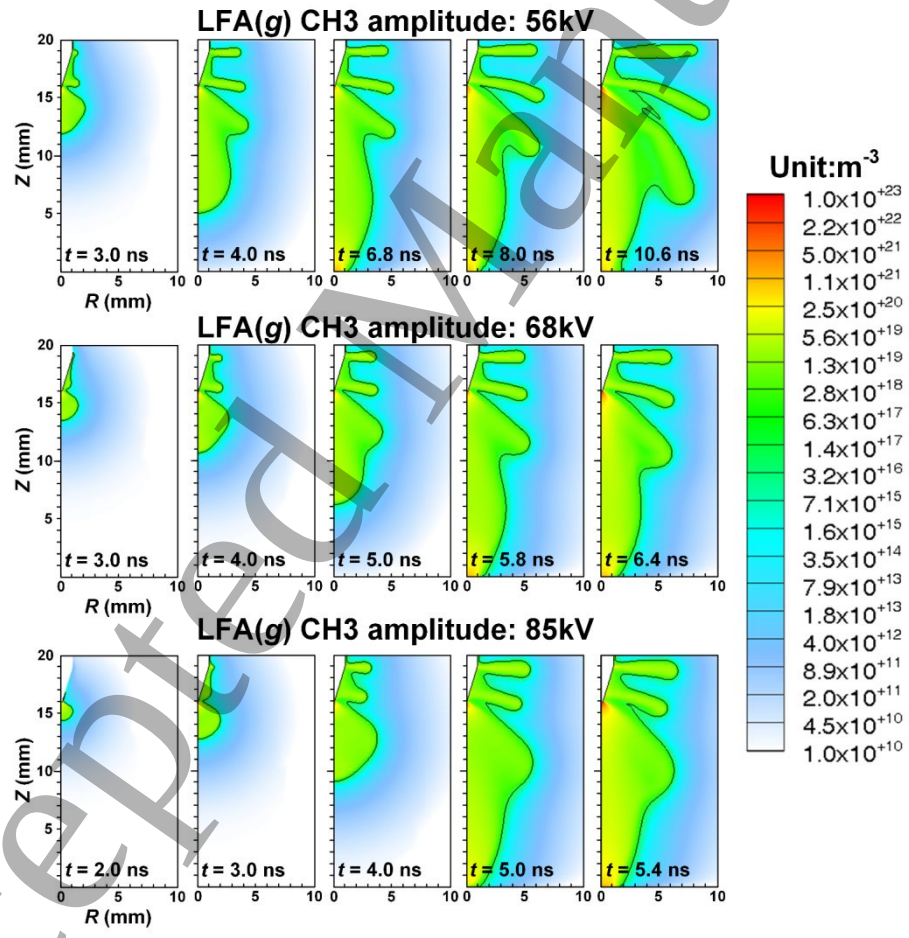

Fig. 10 The electron density distribution in CH3 after introducing the correction factor. To distinguish it from the LFA model results, this result is denoted as LFA(g).

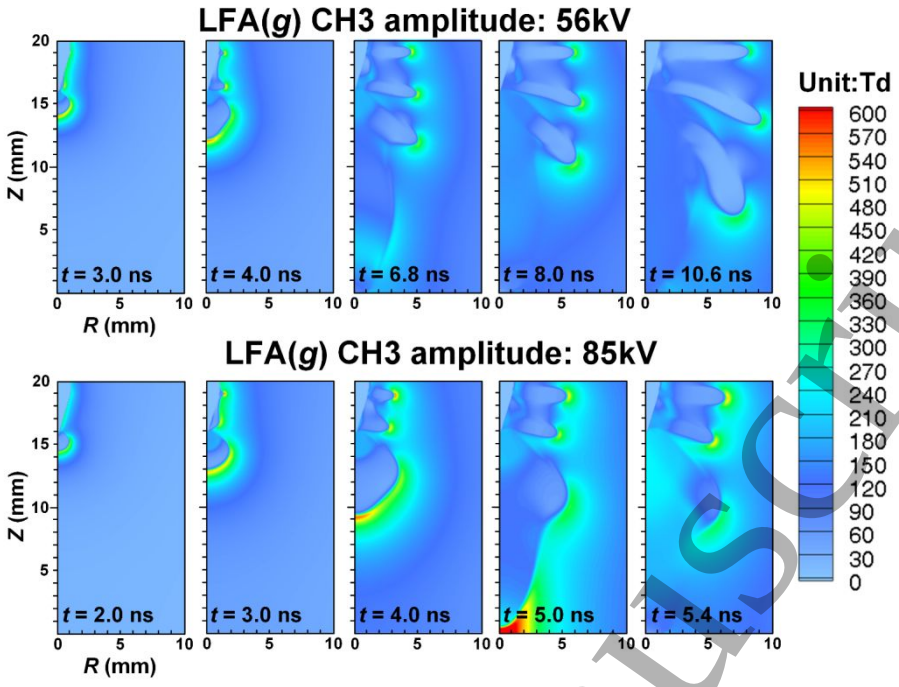

Fig. 11 The reduced electric field distribution in CH3 after introducing the correction factor *g*. To distinguish it from the LFA model results, this result is denoted as LFA(g).

We also investigated the influence of the effective factor *g* on discharge in CH1(2 ns rise time). Fig. 12 presents the simulated electron density evolution and reduced electric field on the axis, the introduction of *g* leads to a lower head electric field (371 Td at *Z*=8 mm). Despite this reduction, after the discharge head reaches *Z*=8 mm, it undergoes a significantly more pronounced acceleration process than the case without the factor(black line in the figure). The head electric field intensifies more as it approaches the plane electrode, ultimately resulting in the discharge reaching the plane electrode earlier (4.6 ns). For reference, in this case, the average E_{ch} of the discharge (the light blue triangular region above the electric field head in Figure 12) is 7.25 kV/cm (29 Td), which is higher than 5.75 kV/cm in LFA and the 4.65 kV/cm stability field.

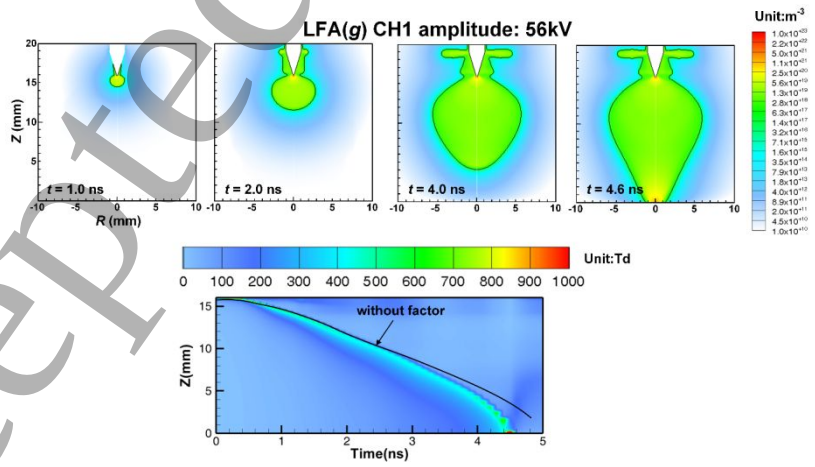

Fig. 12 The electron density and reduced electric field on the axis under 2 ns rise time(CH1). To distinguish it from the LFA model results, this result is denoted as LFA(g).

3.2.4 Investigations on the Local Mean Energy Approximation.

To better describe the 'electron energy cooling process by electric field' mentioned before,

local mean energy approximation(LMEA) is introduced. Particularly, the energy conservation equation for electron energy is solved as shown in equation (3a). In which, n_e is the electron density, ε_m is the mean electron energy, $\mathbf{\Gamma}_\varepsilon$ is the energy flux(expanded form shown in equation(3b), D_ε and μ_ε are the diffusion coefficient and the mobility of the mean electron energy), $P(\varepsilon_m)$ is the electron power loss in collisions(specific expression shown in equation (3c), N_g is the gas density). Under LMEA, both electron swarm data, P_{loss}/N_g, and the rate coefficients for electron impact reactions are expressed as explicit functions of ε_m, given by BOLSIG+.

$$\frac{\partial n_e \varepsilon_m}{\partial t} + \nabla \cdot \mathbf{\Gamma}_\varepsilon = -|q_e| \cdot \mathbf{\Gamma}_e \cdot \boldsymbol{E} - P(\varepsilon_m) \qquad (3a)$$

$$\mathbf{\Gamma}_\varepsilon = -n_e \varepsilon_m \mu_\varepsilon \boldsymbol{E} - D_\varepsilon \nabla(n_e \varepsilon_m) \qquad (3b)$$

$$P(\varepsilon_m) = \frac{P_{loss}}{N_g} \cdot N_g \cdot n_e \qquad (3c)$$

Fig. 13 presents the evolution of electron density and reduced electric field simulated under LMEA in CH3. Its initial and boundary conditions are consistent with those for LFA described in Section 2 and results in Section 3.2.1. The simulation results show completely different results compared to those under LFA: Under 56 kV, the discharge branching process completely disappears, leaving only the main discharge channel. In contrast, the discharge at 85 kV instead exhibits a faint discharge channel branching off from the main discharge channel. This branch is more evident in the electric field distribution shown in the fourth row of Fig. 13. At t=5.5 ns, even when the main discharge channel reaches the plane electrode, a streamer with an enhanced head electric field still exists in space. This situation is largely consistent with the simulation results at 85 kV under LFA after introducing the correction factor g shown in Fig. 11. This phenomenon occurs because the main discharge, generated at higher amplitudes, is wider and more conical in shape(under both LFA and LMEA). This wider discharge creates another electric field peak at its right boundary, distinct from the field at the discharge head (see 85 kV, t=4.0 ns, electric field), which then initiates a separate discharge. Overall, LMEA gives different results from the experimental results, indicating that under these conditions, LMEA does not necessarily yield results consistent with experimental observations. The cause of the differences between LFA and LMEA has been computed in [31]. LMEA accurately calculates both the electron mobility reduction and the diffusion coefficient enhancement process at the discharge head, matching analytical solutions, while the LFA model fails to reproduce this phenomenon. Consequently, diffusion flux and drift flux differ between the two methods, ultimately leading to the more 'subtle' branching phenomenon observed in LMEA.

Fig. 14 shows the discharge development at a 56 kV amplitude in CH1. Compared to the LFA results in Section 3.2.1, its discharge inception time is later, and its average development velocity is slightly faster. This is largely consistent with the LFA(g) results, with both reaching the plane electrode at 4.6 ns. The other difference lies in the maximum width when the discharge reaches the plane electrode: under LMEA, the maximum width is approximately 12 mm (also using the 10^{18} m^{-3} electron density isoline as the discharge contour), whereas in the LFA results, the maximum width is approximately 10.5 mm. As for the electric field at the discharge head, when the discharge propagates through the upper half of the gap (Z=16mm-8mm), there is little difference between LMEA and LFA, with both being around 500 Td. In

the latter half (Z=8mm-2mm), the head electric field under LMEA remains essentially at 450 Td, while under LFA, it decreases to around 360 Td. As it approaches the plane electrode(Z=2mm-0mm), the electric field under LMEA reaches a maximum of over 550 Td, whereas under LFA, the maximum is 500 Td. For reference, in this case, the average internal electric field of the discharge (the light blue triangular region above the electric field head in Figure 14) is 7.5 kV/cm (30 Td), which is higher than 5.75 kV/cm in LFA but similar to the result of LFA(g).

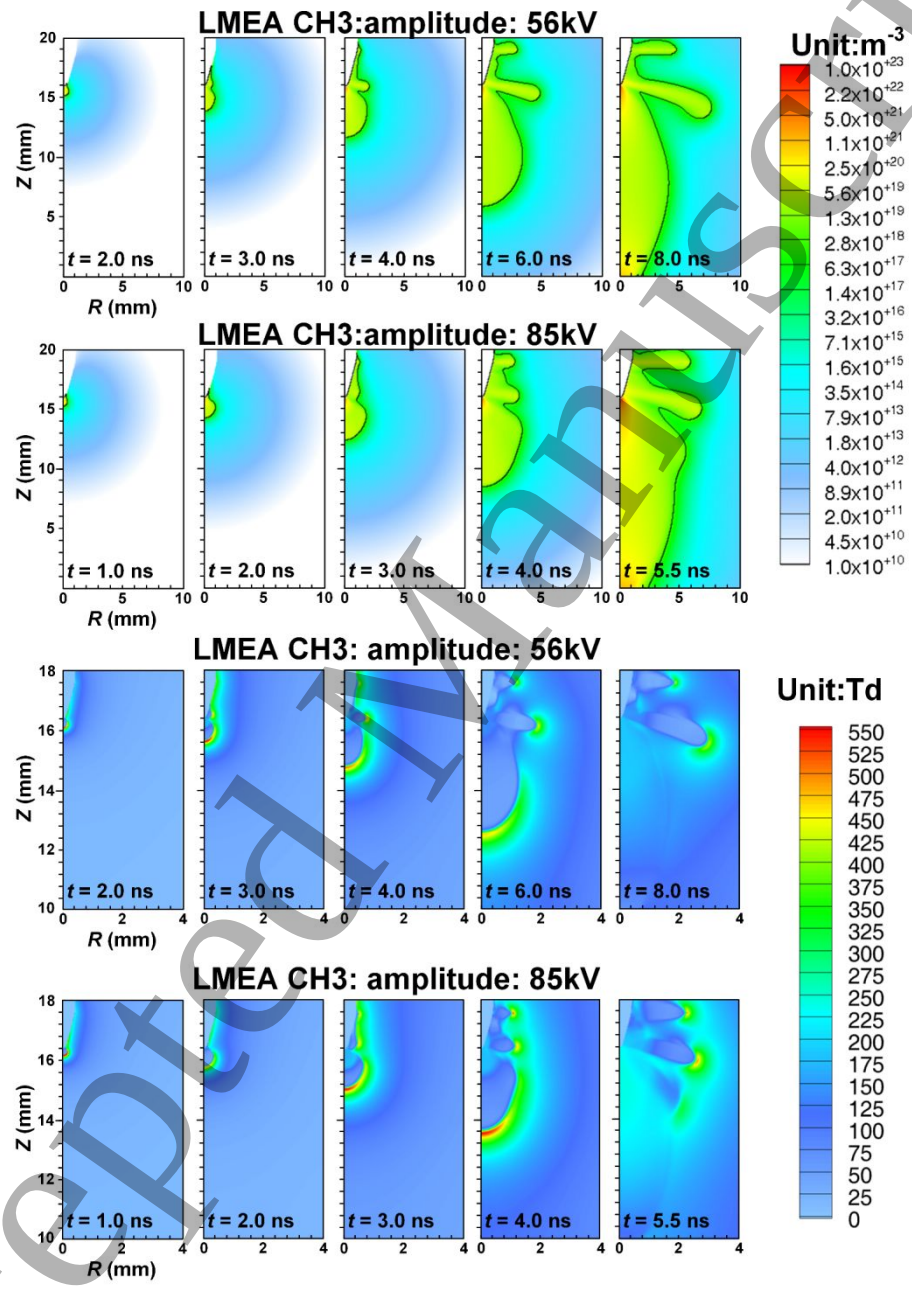

Fig. 13 Electron density and electric field distribution in CH3 under LMEA.

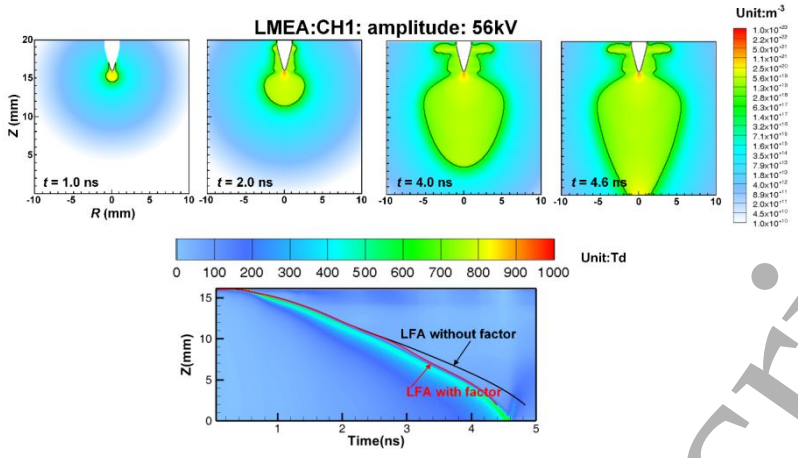

Fig. 14 The electron density and reduced electric field on the axis in CH1 under LMEA.

In addition to the differences in the main discharge, we also observe that the length of the streamer develpoed from the pin surface varies with the model and rise time. Specifically, referring to the discharge development processes at 85 kV shown in Fig. 4, Fig. 6, and Fig. 13, the length of this streamer is summarized in Table 3. Not only the rise time affects the streamer length on the pin surface, but different models also have an influence. However, compared to the main discharge, the model's impact on this streamer length is quite limited. The generation of streamers on the pin surface is due to the strong radial electric field at the pin surface(electric field lines generated are perpendicular to the pin surface), which is similar to the streamer channels created by the discharge branching caused by the strong radial electric field in the main discharge. Therefore, we observe that after introducing LFA(g), the streamer length is significantly reduced compared to LFA and LMEA. Thus, the underlying physical mechanism for this observation aligns with the main discharge.

Table 3. Comparison of streamer length on the pin surface for various rise times and simulation models.

Rise time	Model	Streamer length(mm)
CH1	LFA	3
CH1	LFA(g)	1.8
CH1	LMEA	3.2
CH3	LFA	5.7
CH3	LFA(g)	5.6
CH3	LMEA	6.72

3.2.5 Diffuse discharge under LFA and LMEA: the calculation results comparison

In Section 3.2.4, LMEA simulations show that discharges incept later but propagate faster than in LFA simulations; notably, branched discharges around the main channel also disappear under LMEA. This raises a critical question for non-branching regime diffuse discharges, in CH1: which model, LFA or LMEA, yields results more consistent with experimental observations? This section therefore compares LFA and LMEA simulation results against experimental measurements. It should be emphasized that the discharge optical width in the experiment here can only serve as a reference, as different results may be obtained depending on the criteria for boundary selection, while its discharge breakdown time is fixed. Fig. 15 presents a comparison of the propagation of diffuse discharge length and width obtained from

simulations under LFA, LFA(*g*), and LMEA, at amplitudes of 56 kV and 85 kV in CH1, against those measured experimentally. For the determination of the width and length of the diffuse discharge, we follow the method described in [18]. After performing an Abel inversion on the discharge images, we use the integral of the light emission profile in both directions to determine its width and length. Moreover, in diffuse discharge, the width(optical diameter) is not half of the space charge layer in modeling, as is the case with classic streamers[32, 33], but is close to it. It should be noted that in both experiments and simulations, the discharge incepts only after the voltage is applied for a certain period. However, the time required for discharge inception is not the same in experiments and simulations; generally, the time required in simulations is shorter. To better compare the simulation results, the inception time in the experimental data is shifted according to the time difference between their respective inceptions. This adjustment is to ensure that the discharge size at the moment of inception is not significantly different between the two. At 56 kV, the discharge inception times for LFA and LFA(*g*) are essentially the same, while LMEA is slightly slower by 0.2 ns. However, the times at which LFA(*g*) and LMEA discharges reach the plane electrode are almost identical. This indicates that LMEA has the fastest average development velocity, crossing the entire gap in only 4.2 ns, whereas LFA and LFA(*g*) take 4.7 ns and 4.3 ns, respectively. Overall, LFA(*g*) and LMEA are closer to the experimental results in discharge length. The results for discharge width are opposite: in the LFA results, with a maximum width of 12.31 mm, which is greater than the 11.76 mm and 10.93 mm for LFA(*g*) and LMEA, respectively, and is closest to the experimental value of 12.73 mm. At 85 kV, the inception time for LMEA is also later (by 0.35 ns). It crosses the entire gap in 2.4 ns, whereas LFA and LFA(*g*), although they incept earlier, both require 2.55 ns. These crossing times all differ significantly from the experimental results, with discrepancies of 0.3-0.5 ns. As for the maximum discharge width, the results from all three models are relatively close to the experimental value, around 14.1 mm. Furthermore, at the higher amplitude of 85 kV, the LFA(*g*) and LFA results are more consistent with each other and differ more significantly from the LMEA results. This is reasonable because at higher amplitudes, the discharge develops faster, the head electric field is stronger, and the electron diffusion flux is smaller compared to the drift flux; consequently, the LFA(*g*) and LFA results are largely consistent. It should also be noted that the slower discharge propagation in LFA and the later discharge inception in LMEA are both determined by the characteristics of their respective assumptions. As summarized in the calculations in [31], LFA calculations near electrodes are less reliable compared to LMEA. According to their results, when the discharge approaches the cathode, the sharp increase in electric field strength causes LFA to misestimate diffusion and ionization rates. Before discharge inception, LMEA simulates the decrease in number density due to the absorption of slow electrons by the anode, a phenomenon LFA cannot simulate due to its excessive reliance on the background electric field.

As calculated in [13], the computational accuracy of LFA and LMEA depends not only on the discharge itself but also on the gas pressure and the grid size. For the atmospheric pressure diffuse discharge, the used grid size is 3μm-5μm. This coincidentally falls at the boundary of the computational accuracy for both LMEA and LFA in [13], meaning both can achieve relatively accurate results. By comparison, the calculation results from all three methods are considered relatively close to the experimental results. However, the slow inception time in LMEA leads to a more ‘significant’ discrepancy than LFA and LFA(*g*).

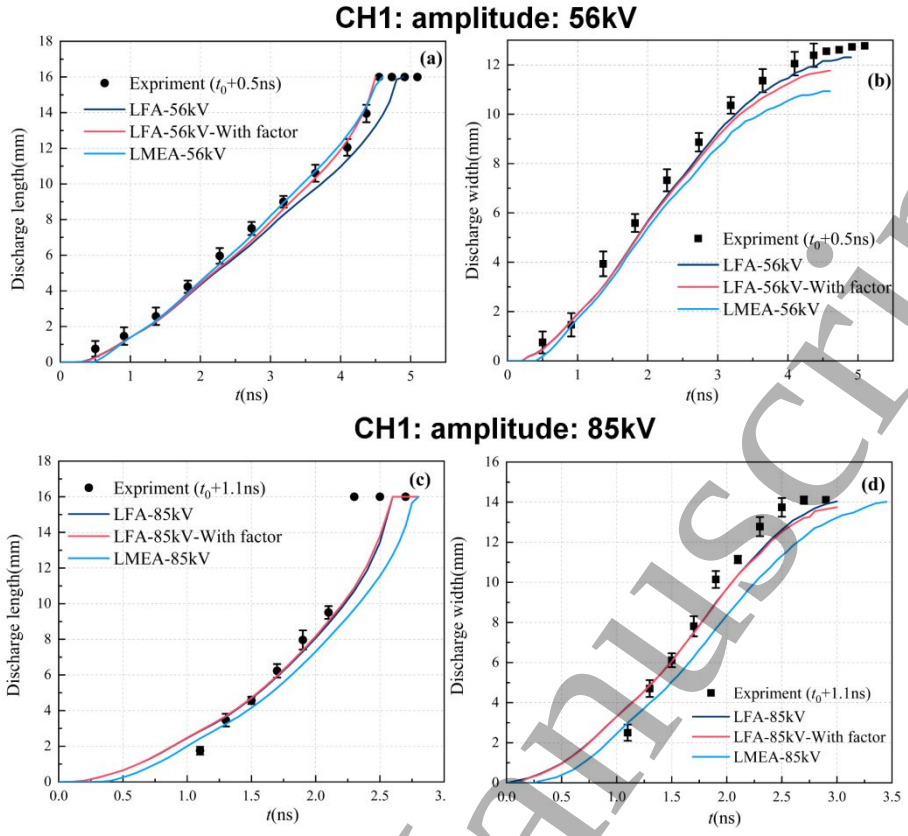

Fig. 15 The diffuse discharge characteristics(length and width) in experiments and simulated results in CH1. The determination of the discharge edge follows the method described in [18]. After performing an Abel inversion on the discharge images, we integrate along the radial and axial directions separately. The 15% value of the maximum integral is taken as the discharge edge. This value has been found suitable as the optical radius for diffuse discharge after comparison.

By comparing the differences in electric fields under different models presented in Fig. 5, Fig. 12, and Fig. 14, with the electron density distributions shown in Fig. 4, Fig. 12, and Fig. 14, we further analyze the calculations of electric field strength and electron density under different models.

Regarding the reduced electric field, the average value of the reduced electric field at the discharge head in LFA is around 400 Td. When the discharge propagates to the electrode center (Z=8 mm), the head electric field is 400 Td. Throughout the propagation process, the average electric field within the discharge is 38 Td. In LFA(g), the average value of the reduced electric field at the head is around 420 Td, and the electric field at Z=8 mm is 417 Td, with an average internal electric field of 44 Td. In LMEA, the average value of the reduced electric field at the head is around 445 Td, the electric field at Z=8 mm is 450 Td, and the average internal electric field is 46 Td. It can be seen that the electric field values obtained from LFA(g) and LMEA are both higher than those from LFA.

Regarding electron density, taking Z=15.8 mm (near the pin electrode) and Z=8 mm (center of the gap) as examples at the moment of discharge breakdown, the electron densities under LFA are 2.3×10^{21} m^{-3} and 2×10^{19} m^{-3}, respectively. Under LFA(g), they are 2.3×10^{21} m^{-3} and 3×10^{19} m^{-3}. Under LMEA, they are 1.8×10^{21} m^{-3} and 3.4×10^{19} m^{-3}. The results given by the

three models show high consistency, with the specific numerical values being quite close.

In regions of high field gradients, such as the streamer head, LFA overestimates the ionization rate as it assumes electrons instantaneously acquire energy from the local field. In contrast, LMEA solves the energy conservation equation, thus necessitating a stronger local electric field to achieve the ionization required for streamer propagation. Despite this difference in the underlying field dynamics. The convergence of the electron density predictions across the models indicates that the structure of the conductive plasma channel is a well-constrained outcome of the discharge.

3.2.5 3D modeling results under LFA

In the above sections, we use a 2D axisymmetric fluid model to investigate diffuse discharge behavior (including branching streamers) under varying voltage rise times and amplitudes. To analyze the branching process of discharges, however, 3D modeling remains the most appropriate approach. As demonstrated in [15], a 3D fluid model with Monte Carlo photoionization can quantitatively simulate branching phenomena in low-pressure streamer discharges. Nevertheless, large-volume diffuse discharges generated by high-amplitude nanosecond pulses at atmospheric pressure require substantially finer spatial resolution-employing 10 μm square grids would necessitate over 10^8 computational elements even with adaptive mesh refinement concentrated on high-field regions near discharge fronts. This imposes prohibitive computational demands. Thus this study exclusively conducts 3D simulations of discharge behavior localized near the pin electrode.

Maintaining consistent boundary and initial conditions with the 2D model, electron density distributions calculated through simple 3D modeling under 56 kV with different voltage rise times are shown in Fig. 16. To better visualize discharge morphology, a linear color bar is employed instead of the logarithmic scale used in previous sections. In CH3 under LFA, similar to 2D axisymmetric results, discharge branching occurs even earlier (at Z=15 mm) yet lacks an experimentally observed main discharge channel. In contrast, the CH1 case maintains spherical diffuse morphology without branching tendencies after 1 mm propagation, but computational constraints prevent full development calculation due to excessive grid requirements. Through simple 3D simulation results, 2D LFA calculation results are close to the experimental results to a certain extent, and are also consistent with the 3D results to a certain extent: under the same amplitude, the discharge tends to branch under long rise time, while maintaining a diffuse morphology under short rise time.

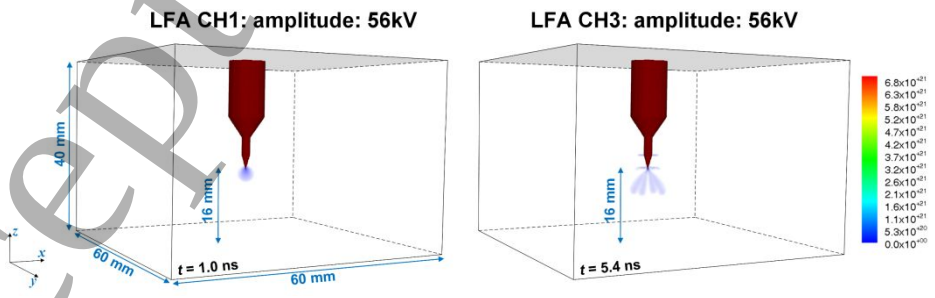

Fig. 16 Electron density distribution under LFA in a simple 3D modeling.

3.2.6 Discussion on runaway electrons

Furthermore, in diffuse discharges, especially at very high overvoltage levels (corresponding to discharges at an 85 kV voltage amplitude in this work), the discharge is likely

to develop from electron avalanches initiated by field-emitted electrons [34, 35]. This further enhances the electrons at the avalanche head and generates runaway electrons, thus making the discharge more diffuse.

As Tarasenko mentioned in the review work [36], the runaway electrons observed in experiments are primarily concentrated in negative polarity streamers (i.e., anode-directed). In contrast, fast electrons are not easily generated at the head of positive polarity streamers. However, their heads can be ionized by X-rays. Similar content is also mentioned in Nijdam et al.'s review work [37], where they also concluded that higher energy electrons are more readily produced in negative polarity discharges. Therefore, for the diffuse discharge process generated under positive polarity in this work, the probability of generating runaway electrons at the discharge head is lower than in negative polarity discharges at the same voltage amplitude. Instead, they are more likely to be generated near the pin surface.

In the computational work of Marode et al. [11], through simple estimations combined with fluid model simulation results, they concluded that runaway electrons may appear near the electrodes in positive polarity diffuse discharges, potentially bombarding the electrodes and producing X-ray radiation. In Brisset's work [38], X-ray radiation detection was performed under the exact same voltage amplitude and electrode setup as in this work. However, the experimental results did not detect any significant X-ray radiation. Although this could be due to the need for improved detector sensitivity, it still reveals that the diffuse discharge process under the same conditions in this work is not accompanied by the generation of runaway electrons.

Fluid models have an inherent disadvantage when calculating runaway electrons. Their assumptions prevent them from accurately simulating discharge processes where runaway electrons play a significant role. This limitation has been highlighted in the computational works of Marode et al. [11] and Dias et al. [39]; both LMEA and LFA are unable to describe this process. To accurately calculate discharge processes under such conditions, only PIC-MCC models or fluid/PIC hybrid models can be used. A typical computational work is that of Ren et al. [40], who used a 2D PIC-MCC model and artificially introduced micro-protrusions to enhance this process, calculating the generation of runaway electrons due to field emission on the electrode surface during negative polarity diffuse discharge.

In summary, it is possible for runaway electrons to be generated near the pin in our positive polarity diffuse discharge in this work. However, the experimental results reveal no significant X-ray radiation. Furthermore, the positive diffuse discharge characteristics obtained from the fluid model simulation in this work are relatively close to those observed experimentally. Therefore, it can be approximately assumed that the fluid model in this work is effective for simulating this positive polarity diffuse discharge process. However, to further investigate the generation and development of runaway electrons, a PIC-MCC model is essential, which is currently outside the scope of this work. In the future, perhaps the development of hybrid models will aid in better calculating this process.

4. Conclusions and outlook

In this work, we investigate the morphological characteristics of positive diffuse discharge under atmospheric pressure fast-rising nanosecond pulse discharges with different voltage amplitudes and rise times using different 2D fluid simulation models (LFA, LFA with

correction factors, and LMEA). We obtain the process by which the discharge gradually transitions from a 'diffuse regime' to a 'multi-channel regime' by decreasing the voltage rise time.

At a 2.0 ns rise time (corresponding to CH1 in the above results), the discharge maintains a diffuse discharge morphology at all voltages from 56-85 kV. Before propagating halfway across the electrode gap, it propagates forward as a spherical shape, and after propagating through the latter half, the discharge head gradually protrudes and propagates in a conical shape. Notably, among the three voltages studied, only the discharge at 56 kV propagates forward at a constant velocity. At amplitudes of 68 kV and 85 kV, the discharge shows significant acceleration after crossing halfway through the electrode gap, which is consistent with the experimental results of Tardiveau *et al* [1]. Through analysis, this is because the internal electric field of the diffuse discharge generated only at 56 kV is close to the stability field in the air.

At a 5.8 ns rise time (corresponding to CH3), the situation becomes more complex, with different models yielding different results. In the LFA model, the discharges at different voltage amplitudes all exhibit a pronounced 'off-axis' phenomenon. As the voltage increases, this branching phenomenon occurs later, but they generally show the same shape. The reason for this phenomenon is that the position of the electric field peaks at the discharge head, under a slow rise time, shifts, deviating from the symmetry axis. Furthermore, this is determined by the characteristics of the applied electric field and the discharge itself and is not caused by computational instability or grid size. During the calculation process, the condition that makes LFA effective is consistently maintained at all times, and no situation arises where the assumption fails. A significant flaw in the LFA results is the absence of a main discharge channel developing along the symmetry axis in the simulation. Yet 3D simulations confirm that such a result is entirely possible. By adjusting the distribution of seed electrons to an elliptical shape, the main discharge channel can appear in the discharge, and this seed distribution is also plausible in experimental conditions. By adopting the full flux scheme correction method to modify the LFA model, more accurate simulation results can be obtained by reducing the diffusion flux of electrons along the parallel electric field. The simulation results with the introduced correction factor indicate that in this situation, the discharge, while maintaining the presence of the main discharge channel, still produces branching discharges that deviate from the main discharge channel. However, by increasing the voltage, the branching becomes less pronounced, which is more consistent with the experimental results. Results after adopting LMEA are slightly closer to those of the corrected LFA, both maintaining the presence of the main discharge channel. However, their discharge branching phenomenon persists at higher voltage amplitudes, which is inconsistent with the experimental results.

Finally, by comparing the results from different models with the highly repeatable diffuse discharge from the experiment, it is found that compared to LFA, the results under LMEA exhibit a generally higher discharge inception delay and a faster discharge development velocity. Overall, the LFA with the introduced correction scheme and LMEA provide simulation results that are closer to the experiment.

Although this work uses an axisymmetric model to simulate the 'multi-channel regime' discharge, there is still a fundamental discrepancy with the actual branching phenomena observed in experiments. However, the overall trend of the discharge transitioning from diffuse to branched is consistent with the experiment. Furthermore, the most suitable 3D simulation

model for this research subject requires a massive computational load due to high gas pressure and strong electric fields, making it nearly impossible to complete. In this work, we compare and validate with a simple 3D simulation model and a 2D axisymmetric model, which preliminarily confirms the reliability of the simulation results. However, a more accurate description of this phenomenon still requires further computation using a 3D model.

Acknowledgments

Project supported by the China Scholarship Council (CSC) (Grant No. 202206280081), the Natural Science Basic Research Program of Shaanxi (No. 2024ZY-JCYJ-01-06), the National Natural Science Foundation of China (Grant No. 52077169), the Fundamental Research Funds for the Central Universities, China (Grant No. xtr052023003, xpt012024063), and the State Key Laboratory of Electrical Insulation and Power Equipment, China (Grant No. EIPE23114). The authors would also like to thank E. Marode for his valuable suggestions.

Appendix A

In the reaction system described above (Table 1), we do not consider the influence of stepwise ionization processes on the discharge. However, in nanosecond pulsed discharges, stepwise ionization may play a significant role, even affecting the overall discharge morphology by influencing the ionization strength. Therefore, based on the original reaction system, we have added the relevant reactions shown in Table A1 to investigate the impact of stepwise ionization reactions on diffuse discharge.

Table A1 Reactions added to the original reaction system*

	Reaction	Reaction rate	Ref
R1	$e+N_2 \rightarrow N_2(A)+e$	$f(\sigma, E/N)$	[21]
R2	$e+N_2 \rightarrow N_2(B)+e$	$f(\sigma, E/N)$	[21]
R3	$e+N_2 \rightarrow N_2(C)+e$	$f(\sigma, E/N)$	[21]
R4	$N_2(B)+ N_2 \rightarrow N_2(A)+ N_2$	10^{-11}	[24]
R5	$N_2(C)+ N_2 \rightarrow N_2+ N_2$	10^{-11}	[24]
R6	$N_2(C) \rightarrow N_2(B)+h\nu$	3×10^{7}	[24]
R7	$N_2(C)+ e \rightarrow N+N+e$	$f(E/N)$	[41]
R8	$N_2(C)+ e \rightarrow N_2(B)+ e$	$f(T_e)$	[41]
R9	$N_2(B)+ e \rightarrow N_2(A)+ e$	$f(T_e)$	[41]
R10	$N_2(A)+ e \rightarrow N_2^+ +e+e$	$f(E/N)$	[42]
R11	$N_2(C)+ e \rightarrow N_2^+ +e+e$	$f(E/N)$	[42]
R12	$N_2(A)+ N_2(A) \rightarrow N_2(C)+ N_2(X)$	1.5×10^{-10}	[24]

*Unit of rate constants are s^{-1}, $cm^3\ s^{-1}$, and $cm^6\ s^{-1}$. T_e is the electron temperature calculated based on BOLSIG+ with cross sections indicated in the table.

Fig. A1 shows the electron density distribution during the discharge process under CH1 and CH3 at a voltage amplitude of 56 kV, both before and after adding the reactions from Table A1. The results indicate that at the same time, the discharge morphologies under the two reaction systems are quite similar. However, the discharge develops slightly faster after adding

the new reaction system. Furthermore, the electron density within the discharge channel is also higher after adding the new reaction system compared to when it was not added.

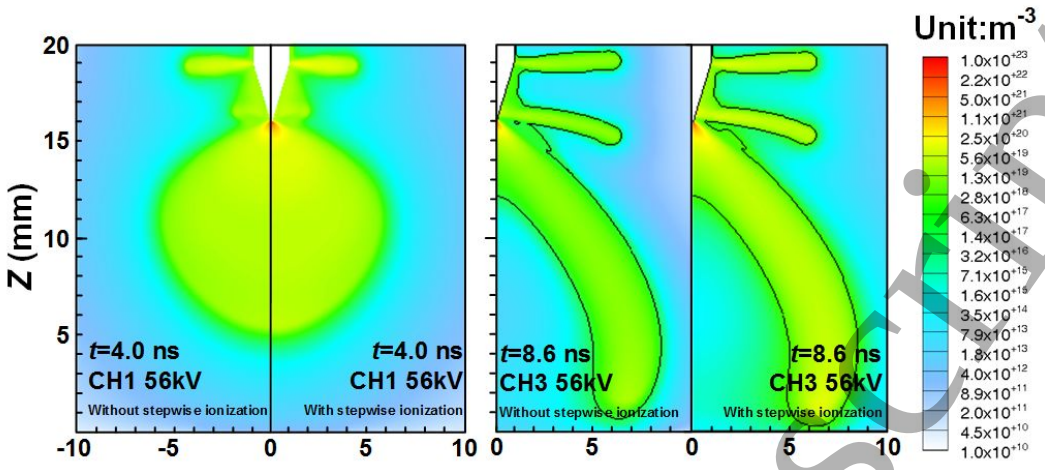

Fig. A1 Electron density distribution of discharge in CH1 and CH3 at a voltage amplitude of 56 kV, with and without the reactions from Table A1. The left side of each subplot shows the results without the added reactions, and the right side shows the results after their addition.

Fig. A2 presents the electron density and reduced electric field strength extracted along the axis at 4.0 ns for the diffuse discharge process at 56 kV under CH1. In terms of electron density, the overall electron density increases after adding the reactions. However, within the discharge channel, although the electron density value increases, the magnitude of the increase is not significant. The most substantial increase occurs at the pin, where the maximum electron density rises from approximately 1×10^{22} m^{-3} to 3×10^{22} m^{-3} after adding the new reactions. Regarding electric field strength, it can be observed that the development speed of the ionization wave front only increases by about 0.1 mm, and the head electric field increases by approximately 5 Td, indicating a relatively small change.

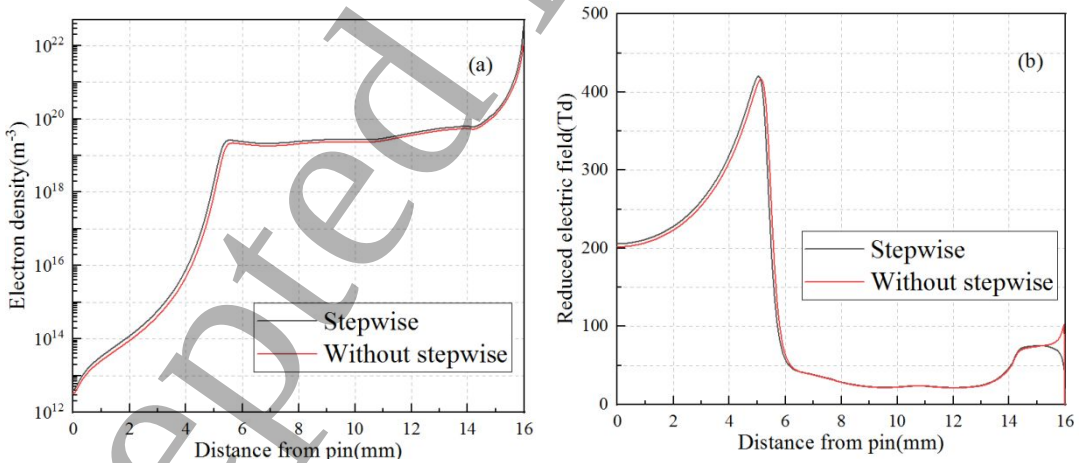

Fig. A2 Electron density and reduced electric field distributions along the axis of diffuse discharge in CH1 at a voltage amplitude of 56 kV, with and without stepwise ionization. (a) is the electron density. (b) is the reduced electric field

In summary, stepwise ionization indeed influences the electron density distribution during the discharge process. Specifically, it results in an overall increase in electron density within the discharge channel, a sharp increase in electron density near the pin electrode, and a slight increase in discharge width. However, the overall discharge morphology does not change

significantly compared to the case without the added reactions. This suggests that the impact of stepwise ionization on diffuse discharge under these conditions is likely limited.

Reference

[1] Tardiveau P, Magne L, Marode E, Ouaras K, Jeanney P and Bournonville B 2016 Sub-nanosecond time resolved light emission study for diffuse discharges in air under steep high voltage pulses *Plasma Sources Science & Technology* **25** 054005

[2] Briels T M P, Kos J, Winands G J J, van Veldhuizen E M and Ebert U 2008 Positive and negative streamers in ambient air: measuring diameter, velocity and dissipated energy *Journal of Physics D-Applied Physics* **41**

[3] Briels T M P, Kos J, van Veldhuizen E M and Ebert U 2006 Circuit dependence of the diameter of pulsed positive streamers in air *Journal of Physics D-Applied Physics* **39** 5201-5210

[4] Chen S, Heijmans L C J, Zeng R, Nijdam S and Ebert U 2015 Nanosecond repetitively pulsed discharges in N₂-O₂ mixtures: inception cloud and streamer emergence *Journal of Physics D-Applied Physics* **48** 175201

[5] Briels T M P, van Veldhuizen E M and Ebert U 2008 Positive streamers in air and nitrogen of varying density: experiments on similarity laws *Journal of Physics D-Applied Physics* **41** 234008

[6] Briels T M P, van Veldhuizen E M and Ebert U 2008 Time resolved measurements of streamer inception in air *Ieee Transactions on Plasma Science* **36** 908-909

[7] Clevis T T J, Nijdam S and Ebert U 2013 Inception and propagation of positive streamers in high-purity nitrogen: effects of the voltage rise rate *Journal of Physics D-Applied Physics* **46**

[8] Tardiveau P, Moreau N, Bentaleb S, Postel C and Pasquiers S 2009 Diffuse mode and diffuse-to-filamentary transition in a high pressure nanosecond scale corona discharge under high voltage *Journal of Physics D-Applied Physics* **42**

[9] Komuro A, Ono R and Oda T 2013 Effects of pulse voltage rise rate on velocity, diameter and radical production of an atmospheric-pressure streamer discharge *Plasma Sources Science & Technology* **22**

[10] Bourdon A, Péchereau F, Tholin F and Bonaventura Z 2021 Study of the electric field in a diffuse nanosecond positive ionization wave generated in a pin-to-plane geometry in atmospheric pressure air *Journal of Physics D-Applied Physics* **54**

[11] Marode E, Dessante P and Tardiveau P 2016 2D positive streamer modelling in NTP air under extreme pulse fronts. What about runaway electrons? *Plasma Sources Science & Technology* **25** 064004

[12] Brisset A, Gazeli K, Magne L, Pasquiers S, Jeanney P, Marode E and Tardiveau P 2019 Modification of the electric field distribution in a diffuse streamer-induced discharge under extreme overvoltage *Plasma Sources Science & Technology* **28** 055016

[13] Zhu Y F, Chen X C, Wu Y, Hao J B, Ma X G, Lu P F and Tardiveau P 2021 Simulation of ionization-wave discharges: a direct comparison between the fluid model and E-FISH measurements *Plasma Sources Science & Technology* **30** 075025

[14] Teunissen J and Ebert U 2016 3D PIC-MCC simulations of discharge inception around a sharp anode in nitrogen/oxygen mixtures *Plasma Sources Science & Technology* **25**

[15] Wang Z, Dijcks S, Guo Y H, van der Leegte M, Sun A B, Ebert U, Nijdam S and Teunissen J 2023 Quantitative modeling of streamer discharge branching in air *Plasma Sources Science & Technology* **32**

[16] Zhu Y F, Shcherbanev S, Baron B and Starikovskaia S 2017 Nanosecond surface dielectric

barrier discharge in atmospheric pressure air: I. measurements and 2D modeling of morphology, propagation and hydrodynamic perturbations *Plasma Sources Science & Technology* **26** 125004

[17] Chen X C, Zhu Y F, Wu Y, Hao J B, Ma X G and Lu P F 2021 Modeling of fast ionization waves in pure nitrogen at moderate pressure *Plasma Sources Science & Technology* **30**

[18] Guo Y L, Li Y R, Zhu Y F and Sun A B 2023 A numerical and experimental study on positive diffusive ionization waves in different N₂/O₂ mixtures: the role of photoionization *Plasma Sources Science & Technology* **32** 025003

[19] CS P 2002 The immersed boundary method *Acta Numerica* **11:479-517**

[20] Li X R, Guo B H, Sun A B, Ebert U and Teunissen J 2022 A computational study of steady and stagnating positive streamers in N₂-O₂ mixtures *Plasma Sources Science & Technology* **31**

[21] Phelps A V and Pitchford L C 1985 ANISOTROPIC SCATTERING OF ELECTRONS BY N-2 AND ITS EFFECT ON ELECTRON-TRANSPORT *Physical Review A* **31** 2932-2949

[22] Lawton S A and Phelps A V 1978 Excitation of the b 1Σ+g state of O2 by low energy electrons *The Journal of Chemical Physics* **69** 1055-1068

[23] Pancheshnyi S 2013 Effective ionization rate in nitrogen-oxygen mixtures *Journal of Physics D-Applied Physics* **46** 155201

[24] Kossyi I A, Kostinsky A Y, Matveyev A A and Silakov V P 1992 Kinetic scheme of the non-equilibrium discharge in nitrogen-oxygen mixtures *Plasma Sources Science & Technology* **1** 207-220

[25] Bourdon A, Péchereau F, Tholin F and Bonaventura Z 2021 Morphology of positive ionization waves in atmospheric pressure air: influence of electrode set-up geometry *Plasma Sources Science & Technology* **30**

[26] van Veldhuizen E M and Rutgers W R 2002 Pulsed positive corona streamer propagation and branching *Journal of Physics D-Applied Physics* **35** 2169-2179

[27] Francisco H, Teunissen J, Bagheri B and Ebert U 2021 Simulations of positive streamers in air in different electric fields: steady motion of solitary streamer heads and the stability field *Plasma Sources Science & Technology* **30**

[28] Teunissen J 2020 Improvements for drift-diffusion plasma fluid models with explicit time integration *Plasma Sources Science & Technology* **29**

[29] Simon G and Botticher W 1994 Two‐dimensional model of the ignition phase of high‐pressure glow discharges *Journal of Applied Physics* **76** 5036-5046

[30] Soloviev V R and Krivtsov V M 2009 Surface barrier discharge modelling for aerodynamic applications *Journal of Physics D Applied Physics* **42** 125208

[31] Grubert G K, Becker M M and Loffhagen D 2009 Why the local-mean-energy approximation should be used in hydrodynamic plasma descriptions instead of the local-field approximation *Physical Review E* **80** 036405

[32] Nudnova M M and Starikovskii A Y 2008 Streamer head structure: role of ionization and photoionization *Journal of Physics D-Applied Physics* **41**

[33] Luque A and Ebert U 2009 Emergence of sprite streamers from screening-ionization waves in the lower ionosphere *Nature Geoscience* **2** 757-760

[34] Mesyats G, Zubarev N and Vasenina I 2020 On the Nature of Nanosecond Diffusion-Channel Discharges in Air *2020 7th International Congress on Energy Fluxes and Radiation Effects*

(EFRE) 1-5

[35] Mesyats G A and Vasenina I V 2021 Characterization of Nanosecond Diffuse-Channel Discharges in Atmospheric Air *Plasma Physics Reports* **47** 907-911

[36] Tarasenko V 2020 Runaway electrons in diffuse gas discharges *Plasma Sources Science & Technology* **29** 034001

[37] Nijdam S, Teunissen J and Ebert U 2020 The physics of streamer discharge phenomena *Plasma Sources Science & Technology* **29** 103001

[38] Alexandra B 2019 Physique des décharges nanosecondes diffuses générées sous champs extrêmes (in French) PhD Thesis Université Paris-Saclay

[39] Dias T C and Guerra V 2025 Are local-field and local-energy approximations appropriate for modeling nanosecond discharges? *Journal of Physics D-Applied Physics* **58**

[40] Ren C H, Huang B D, Zhang C, Qi B, Chen W J and Shao T 2023 The critical effect of electron acceleration under enhanced electric field near cathode on the formation of runaway electrons and diffuse discharge in atmosphere *Plasma Sources Science & Technology* **32** 085013

[41] Bacri J and Medani A 1982 Electron diatomic molecule weighted total cross section calculation: III. main inelastic processes for N2 and N+ 2 *Physica B+ C* **112** 101-118

[42] Dyatko N, Kochetov I and Napartovich A 1992 Electron energy distribution function in a decaying nitrogen plasma *Journal of Plasma Physics* **18** 888-900